High-Resolution NMR in Magnetic Fields with Unknown Spatiotemporal Variations

Philippe Pelupessy, *et al.*

Science **324**, 1693 (2009);
DOI: 10.1126/science.1175102

ductor. On the overdoped side, the nodal gap, on average, tracks the T_c of the sample, although there is strong local inhomogeneity that gives rise to local patches of pairing, even above T_c (*9*, *23*). The data on the underdoped side show that pairing associated with nodal excitations does not increase in strength beyond its value at optimal doping and does not track T_c, yet the angular range of universal nodal *d* wave excitations is systematically suppressed as doping is reduced.

Examination of the temperature evolution of the tunneling spectra across T_c demonstrates an important connection between the universal *d* wave structure we find at low temperatures and the Fermi arc behavior that has long been the hallmark of underdoped cuprates (*13*). The angular extraction procedure for $\Delta(\Theta)$ previously used at low temperature can also be applied to determine the temperature dependence of $\Delta(\Theta)$. Figure 5, A and B, shows the temperature evolution of the extracted $\Delta(\Theta)$ for two underdoped samples (T_c = 58 and 35 K), whereas the insets show the corresponding sample-averaged spectra. As the temperature is raised above T_c, the gaps around the node vanish leading to an arc of gapless excitations, whereas the anti-node is relatively unchanged. The value of the lifetime broadening, Γ, for these fits is determined at the lowest temperature. The destruction of the gap can imply that either the amplitude of the gap is zero or the lifetime broadening exceeds the gap magnitude (*14*, *15*).

Although the nodal gaps disappear above T_c in underdoped samples, the temperature dependence of the gaps is very different from that of a conventional *d* wave BCS superconductor. As the temperature is raised, the nodal points do not reduce continuously as a function of temperature and disappear at T_c, but rather they develop into an arc whose length increases with increasing temperature. The observation of the Fermi arc above T_c is in accord with previous ARPES measurements that ubiquitously show this phenomenon in the underdoped cuprates (*13*, *19*); however, the $\Delta(\Theta)$ from STM measurements shown in Fig. 5 provides a new perspective on the relation between the arc and the *d* wave nodal gap. For both underdoped samples, the angular region over which the arc occurs immediately above T_c is the same as the universal *d* wave region we observed at temperatures well below T_c. As the doping is reduced (the two dopings shown in Fig. 5), both the arc regions as well as the universal *d* wave region decrease together.

Our measurements of the behavior of the nodal gaps with doping and temperature suggest a new picture of superconductivity in BSCCO. In overdoped samples, the nodal gaps, on average, increase with T_c, as one would expect for an inhomogeneous *d* wave superconductor, and collapse at a range of temperatures above T_c, correlating with the local variation of the pairing interaction (*9*, *23*). The anisotropic shape of the gap follows that of a simple *d* wave order parameter, and it is reasonable to assume that the entire Fermi surface contributes to bulk superconductivity. Below optimal doping, the anti-nodal gap continues to increase with decreasing hole doping, as has been measured in several previous experiments (*7*–*10*, *12*, *19*). However, our measurements demonstrate that the nodal gap does not change with reduced doping. The pairing strength does not get weaker or stronger as the Mott insulator is approached; rather, it saturates. There are strong deviations from the universal *d* wave excitation spectrum, which occur closer to the node with reduced doping. For each doping, the deviation point coincides with the Fermi arc observed above T_c. These observations are consistent with the hypothesis that only the areas of the Fermi surface that follow the universal *d* wave spectrum contribute to bulk superconductivity. Such a reduction in the *d* wave region also reduces the superfluid density, which, in turn, could make the systems susceptible to phase fluctuations (*31*), thereby reducing T_c. Although the origin of the anti-nodal gap remains unclear, optimal T_c is achieved when excitations follow the universal *d* wave characteristic along the entire Fermi surface.

References and Notes

1. T. Timusk, B. Statt, *Rep. Prog. Phys.* **62**, 61 (1999).
2. P. A. Lee, N. Nagaosa, X.-G. Wen, *Rev. Mod. Phys.* **78**, 17 (2006).
3. Y. Wang *et al.*, *Phys. Rev. Lett.* **95**, 247002 (2005).
4. V. J. Emery, S. A. Kivelson, J. M. Tranquada, *Proc. Natl. Acad. Sci. U.S.A.* **96**, 8814 (1999).
5. M. R. Norman, D. Pines, C. Kallin, *Adv. Phys.* **54**, 715 (2005).
6. D. LeBoeuf *et al.*, *Nature* **450**, 533 (2007).
7. M. Le Tacon *et al.*, *Nat. Phys.* **2**, 537 (2006).
8. K. Tanaka *et al.*, *Science* **314**, 1910 (2006); published online 15 November 2006 (10.1126/science.1133411).
9. K. K. Gomes *et al.*, *Nature* **447**, 569 (2007).
10. W. S. Lee *et al.*, *Nature* **450**, 81 (2007).
11. M. C. Boyer *et al.*, *Nat. Phys.* **3**, 802 (2007).
12. T. Kondo, R. Khasanov, T. Takeuchi, J. Schmalian, A. Kaminski, *Nature* **457**, 296 (2009).
13. A. Kanigel *et al.*, *Nat. Phys.* **2**, 447 (2006).
14. M. R. Norman, A. Kanigel, M. Randeria, U. Chatterjee, J. C. Campuzano, *Phys. Rev. B* **76**, 174501 (2007).
15. P. W. Anderson, preprint available at http://arxiv.org/abs/0807.0578v1.
16. C.-C. Chien, Y. He, Q. Chen, K. Levin, preprint available at http://arxiv.org/abs/0901.3151.
17. C. Honerkamp, M. Salmhofer, N. Furukawa, T. M. Rice, *Phys. Rev. B* **63**, 035109 (2001).
18. P. W. Anderson, P. A. Casey, preprint available at http://arxiv.org/abs/0902.1980v1.
19. J. C. Campuzano, M. R. Norman, M. Randeria, in *The Physics of Superconductors*, K. H. Bennemann, J. B. Ketterson, Eds. (Springer, Berlin, 2004), pp. 167–265.
20. A. Damascelli, Z. Hussain, Z.-X. Shen, *Rev. Mod. Phys.* **75**, 473 (2003).
21. M. Sutherland *et al.*, *Phys. Rev. B* **67**, 174520 (2003).
22. J. L. Tallon, J. W. Loram, *Physica C* **349**, 53 (2001).
23. A. N. Pasupathy *et al.*, *Science* **320**, 196 (2008).
24. C. Howald, P. Fournier, A. Kapitulnik, *Phys. Rev. B* **64**, 100504 (2001).
25. K. McElroy *et al.*, *Phys. Rev. Lett.* **94**, 197005 (2005).
26. A. Kanigel *et al.*, *Phys. Rev. Lett.* **99**, 157001 (2007).
27. See supporting data on *Science* Online.
28. Y. Kohsaka *et al.*, *Nature* **454**, 1072 (2008).
29. T. Yoshida *et al.*, preprint available at http://arxiv.org/abs/0812.0155v1.
30. R.-H. He *et al.*, *Nat. Phys.* **5**, 119 (2009).
31. V. J. Emery, S. A. Kivelson, *Nature* **374**, 434 (1995).

32. We gratefully acknowledge discussions with P. W. Anderson, N. P. Ong, M. R. Norman, and M. Randeria. The work at Princeton is supported by the U.S. Department of Energy (DOE) under contract DE-FG02-07ER46419 and NSF through the Princeton Center for Complex Materials and through an NSF-Instrumentation grant. The work in BNL is supported by DOE under contract DE-AC02-98CH10886.

Supporting Online Material

www.sciencemag.org/cgi/content/full/1174338/DC1
SOM Text
Figs. S1 to S4
References

31 March 2009; accepted 21 May 2009
Published online 4 June 2009;
10.1126/science.1174338
Include this information when citing this paper.

High-Resolution NMR in Magnetic Fields with Unknown Spatiotemporal Variations

Philippe Pelupessy,[1]* Enrico Rennella,[2] Geoffrey Bodenhausen[1,3]

Nuclear magnetic resonance (NMR) experiments are usually carried out in homogeneous magnetic fields. In many cases, however, high-resolution spectra are virtually impossible to obtain because of the inherent heterogeneity of the samples or living organisms under investigation, as well as the poor homogeneity of the magnets (particularly when bulky samples must be placed outside their bores). Unstable power supplies and vibrations arising from cooling can lead to field fluctuations in time as well as space. We show how high-resolution NMR spectra can be obtained in inhomogeneous fields with unknown spatiotemporal variations. Our method, based on coherence transfer between spins, can accommodate spatial inhomogeneities of at least 11 gauss per centimeter and temporal fluctuations slower than 2 hertz.

Nuclear magnetic resonance (NMR) is arguably one of the most versatile and ubiquitous forms of spectroscopy. Year after year, magnetic resonance imaging (MRI) reveals surprising insights into morphology, function, and metabolism. Most applications, regardless of whether they are concerned with inanimate solids or liquids or with living organisms, rely

on the use of very homogeneous magnetic fields B_0 with spatial variations below about 10^{-9}, so that subtle differences in the environment of various nuclei, leading to chemical shifts and couplings, can be made apparent. However, it is often not possible to work under ideal conditions. For example, sufficiently homogeneous fields are difficult to achieve in ex situ NMR, where the object under investigation is placed outside the magnet (*1*, *2*); in very high fields induced by resistive or hybrid magnets (*3*, *4*); and in samples (including animals and human beings) that are moving because of pulsating arteries or respiration, not to mention discontinuities of magnetic susceptibility due to voids and surgical implants (*5*, *6*).

Many techniques have been proposed to acquire high-resolution spectra under adverse conditions. Spin echoes (*7*, *8*) can refocus the effects of inhomogeneous B_0 fields and reveal couplings that lead to echo modulations (*9*–*11*). If the field's spatial distribution is known, the B_0 inhomogeneity may be compensated by using a radio-frequency (rf) field designed to have a similar, spatially correlated profile. Two such approaches have been described. In the first one, the rf-field $B_1(r)$ profile is designed to match the $B_0(r)$ profile (*12*–*14*). The dephasing caused by the rf field can then be refocused by rephasing in the main B_0 field. In the second approach, the inhomogeneities are compensated by manipulating the phases of the magnetization vectors associated with different voxels in the presence of a known gradient, in the manner of multidimensional single-scan experiments (*15*, *16*). In either case, the field $B_0(r)$ must be time-independent, and its spatial profile must be known, which constitutes a serious handicap.

We obtained high-resolution spectra in inhomogeneous fields by tracking the differences of the precession frequencies (*17*, *18*) of two spins in a single scan, in a way that is closely related to the ultrafast multidimensional experiments developed by Frydman and co-workers (*19*) and improved in our laboratory (*20*). The experiment functions regardless of the B_0 field profile. Spatial inhomogeneities of at least 11 G/cm can be accommodated. This corresponds to a frequency distribution of about 42 kHz (or 70 ppm for a 600-MHz resonance frequency) for a spherical sample 1 cm in diameter. Combining this technique with the *J*-modulated detection scheme of Giraudeau and Akoka (*21*) adds a second dimension that reveals multiplets due to scalar couplings.

As in the two-dimensional (2D) single-scan experiments, the evolution under the chemical shifts needs to be intertwined with gradient encoding (*22*). Let *S* and *I* constitute a homonuclear pair of spins. When a linearly swept adiabatic refocusing pulse is applied in the presence of a gradient to a coherence S_+ with coherence order $p = +1$ belonging to the manifold of *S*-spin transitions (Fig. 1A), the resulting phase at time t_1 is given by

$$\varphi_1 = \alpha\{\Omega_S + \delta\omega(r) + \Gamma_E(r)\}^2 \qquad (1)$$

(*20*), where Ω_S is the chemical shift of the *S* spin, $\delta\omega(r) = -\gamma_S B_0(r)$ is the (unknown) spatially dependent frequency induced by the inhomogeneous B_0 field, $\Gamma_E(r) = \gamma_S \mathbf{G}_E \cdot r$ is the (known) frequency induced by the encoding gradient $\mathbf{G}_E = \{G_{Ex}\mathbf{k}, G_{Ey}\mathbf{i}, G_{Ez}\mathbf{j}\}$, and $\alpha = \tau_{ad}/\Delta\omega_{ad}$ is the ratio of the duration τ_{ad} and sweep width $\Delta\omega_{ad}$ of the adiabatic inversion pulse. A second identical pulse combined with an opposite gradient then leads to a phase at time t_2:

$$\varphi_2 = 4\alpha\{\Omega_S + \delta\omega(r)\}\Gamma_E(r) \qquad (2)$$

The coherence can then be transferred (in the example of Fig. 1 by a simple $\pi/2$ pulse) from S_+ to I_- with coherence order $p = -1$ through any spin-spin coupling, exploiting (for example) a scalar interaction J_{IS}. If there are no scalar couplings, it might be possible to use demagnetizing fields, which can manifest themselves as intermolecular dipolar interactions (*23*, *24*). After an identical block comprising two more pulses and gradients, the total accumulated phase at time t_4 will be

$$\varphi_4 = 4\alpha\{\Omega_S + \delta\omega(r)\}\Gamma_E(r) - 4\alpha\{\Omega_I + \delta\omega(r)\}\Gamma_E(r) = 4\alpha\{\Omega_S - \Omega_I\}\Gamma_E(r) \qquad (3)$$

This phase does not depend on the spatial variation $\delta\omega(r)$ due to the inhomogeneous static field. The phase φ_4 can be refocused by a decoding gradient G_D. A gradient echo will be formed at an instant in time that will be delayed in proportion to the difference $\Omega_S - \Omega_I$

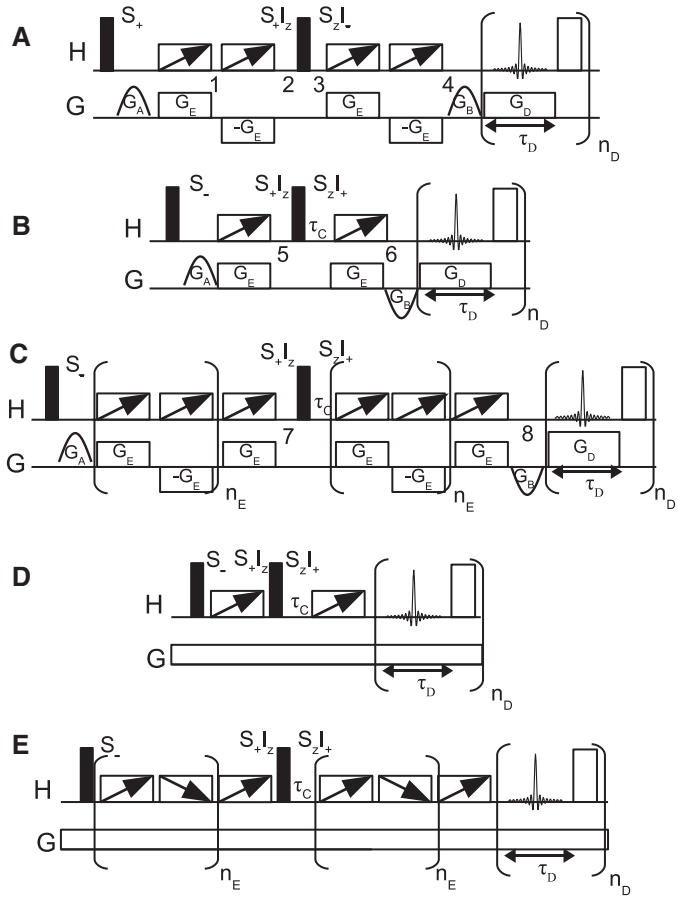

Fig. 1. Pulse sequences to obtain high-resolution spectra in a single scan in arbitrarily inhomogeneous, slowly fluctuating magnetic fields with unknown spatiotemporal distributions. Solid and open vertical rectangles represent $\pi/2$ and π pulses. The rectangles with sloping arrows indicate adiabatic frequency-swept refocusing pulses. G_E and G_D are encoding and decoding gradients. The gradients G_A and G_B of equal area serve to select the desired coherence pathways [they must be identical for (**A**) and opposite for (**B**) and (**C**)]. The delay τ_C serves to compensate for the evolution under the inhomogeneous B_0 field during G_A and G_B. Increasing G_B and prolonging τ_C by $\tau_D/2$ shifts the signals at zero frequency toward the center of the gradient G_D. Sequences (**D**) and (**E**) are adaptations of (B) and (C), respectively, for situations where a permanent gradient is dominant. Adiabatic pulses with down-pointing arrows have reversed sweep directions. The phases of the π pulses during decoding are alternated between x and $-x$ every two pulses (*21*). In these examples, $\pi/2$ pulses are used to achieve transfer of coherence, so that the spins need to be scalar-coupled. Other sequences can be used, such as total correlation spectroscopy (TOCSY). The signals during even (or odd) decoding gradients are arranged in sequential order to yield a 2D array. The gradient echoes that are formed during each decoding gradient appear in a temporal sequence that corresponds to the peaks in the spectrum. The scalar coupling pattern in the other dimension is obtained by performing a Fourier transformation as a function of the index of the decoding gradients.

[1]Département de Chimie Associé au CNRS, Ecole Normale Supérieure, 24 rue Lhomond, 75231 Paris Cedex 05, France. [2]Department of Biomedical Sciences and Technologies, Università degli Studi di Udine, I-33100 Udine, Italy. [3]Institut de Sciences et Ingénierie Chimiques, Ecole Polytechnique Fédérale de Lausanne, Batochime, 1015 Lausanne, Switzerland.

*To whom correspondence should be addressed. E-mail: philippe.pelupessy@ens.fr

between the frequencies of spins S and I. Although this feature is reminiscent of zero-quantum spectroscopy, it should be noted that the echoes arise simply from the differential evolution of two single-quantum coherences (*18*). During the decoding gradient G_D in the scheme of Fig. 1A, the coherences will continue to precess under the field inhomogeneities, thus preventing complete refocusing. An improved scheme is shown in Fig. 1B. Instead of applying two adiabatic pulses before and after coherence transfer, only one is applied, which leads to a phase:

$$\varphi_6 = \alpha\{\Omega_S + \delta\omega(r) + \Gamma_E(r)\}^2 - \alpha\{\Omega_I + \delta\omega(r) + \Gamma_E(r)\}^2 = \alpha\Omega_S^2 - \alpha\Omega_I^2 + 2\alpha(\Omega_S - \Omega_I)\{\Gamma_E(r) + \delta\omega(r)\} \quad (4)$$

The difference $\Omega_S - \Omega_I$ between the chemical shifts of spins I and S is now encoded not only by the gradient G_E but also by the B_0 inhomogeneity. During a decoding gradient G_D with the same amplitude as the encoding gradient G_E, the phase is then

$$\varphi_D(t_D) = \alpha\Omega_S^2 - \alpha\Omega_I^2 + 2\alpha(\Omega_S - \Omega_I)\{\Gamma_E(r) + \delta\omega(r)\} - t_D\{\Omega_I + \Gamma_E(r) + \delta\omega(r)\} \quad (5)$$

At $t_D = 2\alpha(\Omega_S - \Omega_I)$, an echo results because the phase is independent of $\delta\omega(r)$. Thus, a spectrum of frequency differences is obtained in the time domain in a single scan. The phase of this echo is

$$\varphi_D\{t_D = 2\alpha(\Omega_S - \Omega_I)\} = \alpha\Omega_S^2 + \alpha\Omega_I^2 - 2\alpha\Omega_I\Omega_S = \alpha(\Omega_S - \Omega_I)^2 \quad (6)$$

A hybrid scheme is shown in Fig. 1C. A bipolar gradient pair with adiabatic pulses that is repeated n_E times is inserted before each adiabatic pulse of Fig. 1B. The resulting phase at time t_7 is

$$\varphi_7 = 2n_E\alpha(\Omega_S - \Omega_I)\Gamma_E(r) + \alpha\Omega_S^2 - \alpha\Omega_I^2 + 2\alpha(\Omega_S - \Omega_I)\{\Gamma_E(r) + \delta\omega(r)\} = \alpha\Omega_S^2 - \alpha\Omega_I^2 + 2\alpha(\Omega_S - \Omega_I)\{(2n_E + 1)\Gamma_E(r) + \delta\omega(r)\} \quad (7)$$

The decoding gradient should have an amplitude that is $(2n_E + 1)$ times the encoding gradient—$G_D = (2n_E + 1)G_E$—in order to cancel the effects of the inhomogeneities $\delta\omega(r)$. The sequence of Fig. 1C is less sensitive to translational diffusion than the experiment of Fig. 1B (*25*).

As can be seen from Eq. 5, the scheme shown in Fig. 1B does not require any switched field gradients, provided the inhomogeneities are sufficiently large to cause sharp echoes. This

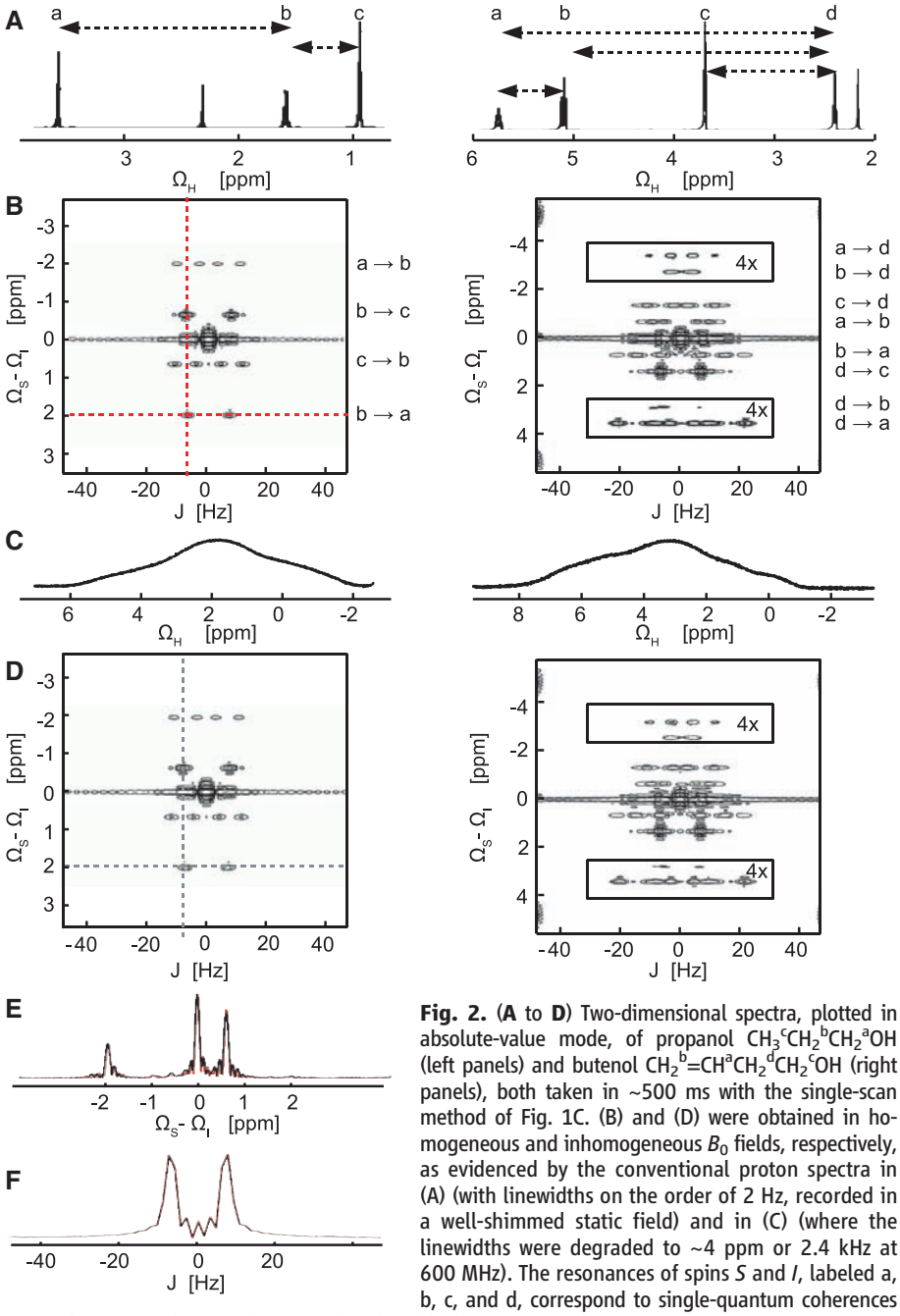

Fig. 2. (**A** to **D**) Two-dimensional spectra, plotted in absolute-value mode, of propanol $CH_3^cCH_2^bCH_2^aOH$ (left panels) and butenol $CH_2^b{=}CH^aCH_2^dCH_2^cOH$ (right panels), both taken in ~500 ms with the single-scan method of Fig. 1C. (B) and (D) were obtained in homogeneous and inhomogeneous B_0 fields, respectively, as evidenced by the conventional proton spectra in (A) (with linewidths on the order of 2 Hz, recorded in a well-shimmed static field) and in (C) (where the linewidths were degraded to ~4 ppm or 2.4 kHz at 600 MHz). The resonances of spins S and I, labeled a, b, c, and d, correspond to single-quantum coherences that evolve during the encoding and decoding blocks of Fig. 1; their scalar coupling patterns appear along the horizontal dimension and carry the same labels ($S \rightarrow I$). The arrows in (A) indicate all difference frequencies between scalar-coupled spins that can be observed; the top arrows correspond to the outer lines in the spectrum, the bottom arrows to the smallest frequency differences (inner lines). The line at zero frequency corresponds to coherences that are refocused but not transferred from one spin to another. Both spectra were recorded with $n_E = 1$, gradients applied simultaneously along directions z and y with strengths $G_E = 0.8$ G/cm and $G_D = 2.4$ G/cm. The adiabatic pulses of 6 ms had a wideband uniform rate and smooth truncation (WURST) profile (*28*) and sweep widths of 14 and 20 kHz for propanol and butenol, respectively. (**E**) Columns taken parallel to the vertical t_1 or ω_1 domain, taken along the dotted lines of the 2D spectra of propanol in homogeneous (red lines) and inhomogeneous fields (black lines), showing differences of chemical shifts in the spectrum of propanol. (**F**) Rows taken parallel to the horizontal ω_2 domain, showing a multiplet due to scalar couplings with a full width at half height of 3.5 Hz, for $n_D = 64$ ($t_2^{max} = 337$ ms).

could have implications for measurements in stray magnetic fields (*26*) or other permanent gradients. Shown in Fig. 1, D and E, are adaptations of Fig. 1, B and C, for situations with a permanent gradient. In Fig. 1E the sweep direction of the second adiabatic pulse in each repeated block is inverted. Both schemes lead to a phase φ_6 of Eq. 4, but the latter limits losses due to diffusion (*25*).

All schemes can be extended from one to two dimensions by appending n_D repetitions of a block comprising a decoding gradient followed by a π pulse in order to observe a train of spin echoes (*21*). A Fourier transformation of this echo train reveals (convoluted) multiplets due to scalar couplings in a second dimension. This option requires ~500 instead of ~50 ms for the basic 1D experiment. The simplest 1D spectrum corresponds to the signal acquired during the first decoding gradient.

Shapira *et al*. (*4*) proposed schemes for measurements in fluctuating resistive magnets. The resolution of correlation spectra can be improved, either by compensating for (known) inhomogeneities with tailored rf fields, or by exploiting echoes following coherence transfer from carbon-13 to proton nuclei. The latter scheme is related to our method, although in their case the effects of inhomogeneities are canceled only at one point in the acquisition period.

The experiments of Fig. 1C have been tested by applications to samples containing 5% 1-propanol ($CH_3CH_2CH_2OH$) and 5% 3-buten-1-ol (CH_2=$CHCH_2CH_2OH$, henceforth simply called butenol) in $CDCl_3$. The spectra in Fig. 2, A and B, have been obtained in a carefully shimmed homogeneous field. The resonances labeled a through d give rise to combination lines (differences in chemical shifts, i.e., four peaks in propanol and eight in butenol). In the vertical dimension, the spectra are symmetric with respect to $\omega_1 = 0$, because each transfer from spin *S* to *I* is accompanied by a transfer in the opposite direction. The central peak at $\omega_1 = 0$ arises from magnetization that is refocused but not transferred from one spin to another.

Shown in Fig. 2, C and D, are spectra obtained with the same method in an inhomogeneous field after deliberately missetting the shim currents. Yet the results of our single-scan experiments are virtually indistinguishable. The experiments have been repeated using several shim settings, invariably leading to similar spectra, as can be seen from the cross sections in Fig. 2, E and F. As with all 2D single-scan experiments, the signal-to-noise ratio decreases in proportion to the square root of the number of points observed in the indirect dimension, relative to a 1D spectrum taken under properly shimmed conditions. If the signal-to-noise ratio is poor, the experiments can be repeated for signal averaging, even if the B_0 inhomogeneities vary in time, provided the fluctuations are slow relative to the time it takes to acquire each scan. For a simple 1D spectrum, about 50 ms is sufficient. Thus, if we assume that the information must be acquired within 10% of the period of the fastest fluctuations, the spectrum of the stochastic variations must be limited to 2 Hz. This should be useful for NMR spectra obtained in resistive Bitter or hybrid magnets, which suffer from random fluctuations due to the power supply and to low-frequency vibrations associated with the circulation of cooling water.

The resolution, as measured by the full linewidth at half height in the vertical (chemical shift) dimension (t_1 or ω_1) of 1-propanol in Fig. 2E, is 60 μs, for a decoding gradient G_D of 4 ms. This corresponds to a resolution of 76 Hz (0.13 ppm) over a frequency range of ±2500 Hz (±4.2 ppm). The resolution of the spectra can be improved by increasing the amplitudes of both encoding and decoding gradients (provided the frequency sweep of the adiabatic pulses covers the frequency range induced by the encoding gradients) or, as shown in Fig. 3, by increasing n_E and the strength of the decoding gradients. The frequency range can be increased by extending the sweep width of the adiabatic pulses, albeit at the expense of the resolution, unless one also increases the strength of both encoding and decoding gradients (*27*). The resolution in the ω_2 dimension is determined by the number n_D of points acquired in the t_2 dimension, as in other forms of 2D spectroscopy.

To mimic a gradient that cannot be switched off, we have applied the scheme of Fig. 1D in the presence of a permanent gradient, or more accurately, a pulsed field gradient that was switched on before the experiment and stopped immediately after observing the signals. The echo corresponding to zero frequency appears at a delay τ_C after the start of signal acquisition. Only 1D spectra revealing combinations of chemical shifts in propanol were recorded (to avoid using prolonged strong gradients). The sample height was decreased to 18 mm, so that the line shape was further deteriorated by susceptibility effects at the edges. Figure 4A shows the resulting spectra in the presence of a gradient G_z = 2.75 G/cm (~35 ppm or 21 kHz across the sample). Signals arising from coherence transfer are indicated by arrows. The duration of the adiabatic pulses was 18 ms and their sweep width was 40 kHz. When the gradient strength was doubled to 5.5 G/cm (~70 ppm or ~42 kHz) together with a doubling of the adia-

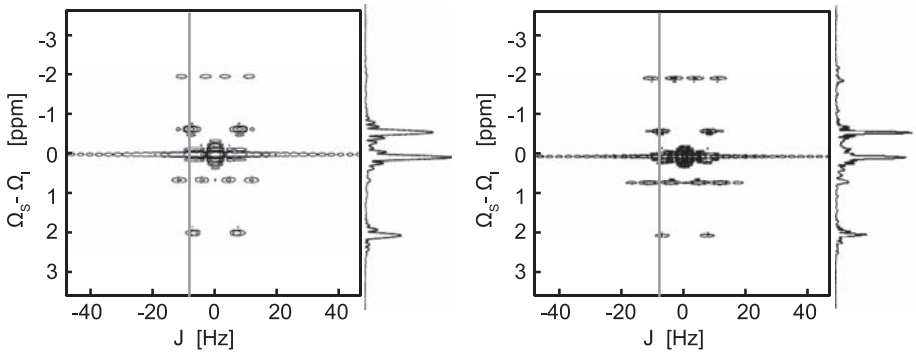

Fig. 3. Left panel: Same spectrum as in the left part of Fig. 2D, taken with n_E = 1 and G_D = 2.4 G/cm. Right panel: Spectrum taken under the same conditions, except that n_E = 2 and G_D = 4 G/cm. The columns shown on the right exemplify the gain in resolution that can be obtained by increasing the number of encoding gradients. The linewidth has improved from 76 Hz (0.13 ppm) on the left to 41 Hz (0.07 ppm) on the right.

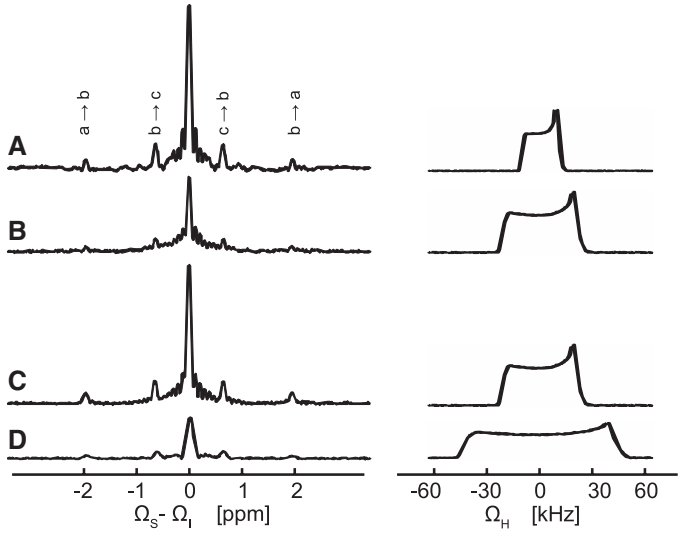

Fig. 4. (**A**) Spectrum of propanol recorded with the method shown in Fig. 1D, with a permanent gradient of 2.75 G/cm applied along the *z* axis throughout the entire sequence, without switching the decoding or encoding gradients. The adiabatic rf pulses had durations of 18 ms and sweep widths of 40 kHz. (**B**) Same as (A), but with twice the amplitude of the permanent gradient (5.5 G/cm) and twice the rf sweep width. (**C**) Same as (B), but each adiabatic pulse is replaced by three 6-ms adiabatic pulses as in Fig. 1E. (**D**) Same as (C), but with a permanent gradient of 11 G/cm and twice the sweep width of the adiabatic pulses. On the right are the corresponding single-quantum spectra.

batic sweep width, there was some loss of intensity due to diffusion (Fig. 4B). These losses could be reduced with the scheme of Fig. 1E, as shown in Fig. 4C for a total of six adiabatic pulses of 6-ms duration (instead of two otherwise identical pulses of 18 ms each, as in Fig. 4B). The linewidth in Fig. 4C is about 70 Hz. Increasing the gradient strength further to 11 G/cm (~140 ppm or ~84 kHz) led to the spectrum in Fig. 4D. In this case, the signal amplitude suffers not only from diffusion losses, but also from the limited rf amplitude (25 kHz) of the initial $\pi/2$ pulse. In stronger gradients, one should use a large number of short inversion pulses that cover a very broad bandwidth with the desired phase profile. In addition, the (possibly frequency-swept) $\pi/2$ pulses should excite the full bandwidth uniformly, bearing in mind that a linear dependence of the phase with respect to offset is allowed.

References and Notes

1. G. Eidmann, R. Savelsberg, P. Blumler, B. Blümich, *J. Magn. Reson. A* **122**, 104 (1996).
2. B. Blümich, J. Perlo, F. Casanova, *Prog. Nucl. Magn. Reson. Spectrosc.* **52**, 197 (2008).
3. Y.-Y. Lin *et al.*, *Phys. Rev. Lett.* **85**, 3732 (2000).
4. B. Shapira, K. Shetty, W. W. Brey, Z. Gan, L. Frydman, *Chem. Phys. Lett.* **442**, 478 (2007).
5. I. J. Cox *et al.*, *J. Magn. Reson.* **70**, 163 (1986).
6. C. E. Mountford, S. Doran, C. L. Lean, P. Russell, *Chem. Rev.* **104**, 3677 (2004).
7. E. L. Hahn, *Phys. Rev.* **80**, 580 (1950).
8. H. Y. Carr, E. M. Purcell, *Phys. Rev.* **94**, 630 (1954).
9. E. L. Hahn, D. E. Maxwell, *Phys. Rev.* **88**, 1070 (1952).
10. R. L. Vold, S. O. Chan, *J. Chem. Phys.* **53**, 449 (1970).
11. R. Freeman, H. D. W. Hill, *J. Chem. Phys.* **54**, 301 (1971).
12. C. A. Meriles, D. Sakellariou, H. Heise, A. J. Moulé, A. Pines, *Science* **293**, 82 (2001).
13. V. Demas *et al.*, *Concepts Magn. Reson. B* **29B**, 137 (2006).
14. J. Perlo *et al.*, *Science* **308**, 1279 (2005); published online 7 April 2005 (10.1126/science.1108944).
15. B. Shapira, L. Frydman, *J. Am. Chem. Soc.* **126**, 7184 (2004).
16. B. Shapira, L. Frydman, *J. Magn. Reson.* **182**, 12 (2006).
17. A. Wokaun, R. R. Ernst, *Chem. Phys. Lett.* **52**, 407 (1977).
18. K. Nagayama, K. Wüthrich, R. R. Ernst, *Biochem. Biophys. Res. Commun.* **90**, 305 (1979).
19. L. Frydman, T. Scherf, A. Lupulescu, *Proc. Natl. Acad. Sci. U.S.A.* **99**, 15858 (2002).
20. P. Pelupessy, *J. Am. Chem. Soc.* **125**, 12345 (2003).
21. P. Giraudeau, S. Akoka, *J. Magn. Reson.* **186**, 352 (2007).
22. L. Frydman, A. Lupulescu, T. Scherf, *J. Am. Chem. Soc.* **125**, 9204 (2003).
23. S. Vathyam, S. Lee, W. S. Warren, *Science* **272**, 92 (1996).
24. G. Galiana, R. T. Branca, W. S. Warren, *J. Am. Chem. Soc.* **127**, 17574 (2005).
25. P. Giraudeau, S. Akoka, *J. Magn. Reson.* **195**, 9 (2008).
26. P. J. McDonald, *Prog. Nucl. Magn. Reson. Spectrosc.* **30**, 69 (1997).
27. P. Pelupessy, L. Duma, G. Bodenhausen, *J. Magn. Reson.* **194**, 169 (2008).
28. E. Kupce, R. Freeman, *J. Magn. Reson. A* **115**, 273 (1995).

29. Supported by CNRS, the Agence Nationale pour la Recherche, the Integrated Infrastructure Initiative (I3) of the 6th Framework Program of the EC (contract RII3-026145, EU-NMR), the Fonds National de la Recherche Scientifique (Switzerland), and the Commission pour la Technologie et l'Innovation (Switzerland).

17 April 2009; accepted 14 May 2009
10.1126/science.1175102

White Phosphorus Is Air-Stable Within a Self-Assembled Tetrahedral Capsule

Prasenjit Mal,[1] Boris Breiner,[1] Kari Rissanen,[2] Jonathan R. Nitschke[1]*

The air-sensitive nature of white phosphorus underlies its destructive effect as a munition: Tetrahedral P_4 molecules readily react with atmospheric dioxygen, leading this form of the element to spontaneously combust upon exposure to air. Here, we show that hydrophobic P_4 molecules are rendered air-stable and water-soluble within the hydrophobic hollows of self-assembled tetrahedral container molecules, which form in water from simple organic subcomponents and iron(II) ions. This stabilization is not achieved through hermetic exclusion of O_2 but rather by constriction of individual P_4 molecules; the addition of oxygen atoms to P_4 would result in the formation of oxidized species too large for their containers. The phosphorus can be released in controlled fashion without disrupting the cage by adding the competing guest benzene.

Microenvironment alters behavior in chemical systems; encapsulation within the inner phase (*1*–*3*) of a molecular container can accelerate a reaction (*4*–*7*), change a reaction's course (*7*–*11*), perturb equilibria (*11*–*13*), or prevent the oligomerization of a reactive species such as a cyclotrisiloxane (*14*) or cyclobutadiene (*15*). The lifetimes of such fleeting molecules as hemiaminals (*16*), benzyne (*17*), and cycloheptatriene (*18*) may also be extended long enough to permit spectroscopic observation. Here, we show how encapsulation can render molecules of white phosphorus (P_4) air-stable through a constrictive mechanism.

The P-P bonds of tetrahedral P_4 (white phosphorus) are weak (200 kJ mol^{-1}) (*19*), leading to a low activation barrier to oxidation, and the P-O bonds of combustion products are strong (330 to 650 kJ mol^{-1}) (*19*), releasing substantial energy during their formation. P_4 is thus violently pyrophoric; its slow chemiluminescent combustion when O_2 is limited ["phosphorescence," the meaning of which has since changed (*20*)] defined the element's essence for the first chemists.

We have described the preparation of tetrahedral cage **1** in aqueous solution from the subcomponents shown in Fig. 1 (*21*). When an aqueous solution of **1** was left in contact with solid white phosphorus, uptake of P_4 converted **1** into the host-guest complex $P_4\subset$**1** (Fig. 1) (*22*). Vapor diffusion of acetone into an aqueous solution yielded crystalline $P_4\subset$**1** in 91% yield.

Incorporation of P_4 into **1** was marked by changes in the ^{1}H nuclear magnetic resonance (NMR) chemical shifts of **1** (fig. S1) and by the appearance of a single resonance in the ^{31}P NMR spectrum at –510 parts per million (ppm). Single crystals of sufficient quality for x-ray diffraction were grown by vapor diffusion of 1,4-dioxane into an aqueous solution of $P_4\subset$**1**. Its x-ray crystal structure is shown in Fig. 2.

The quality and resolution of the diffraction data, although limited, allow for unambiguous assignment of the cage's conformation and the placement of the guest within the cage, where it is disordered between two orientations (only one of

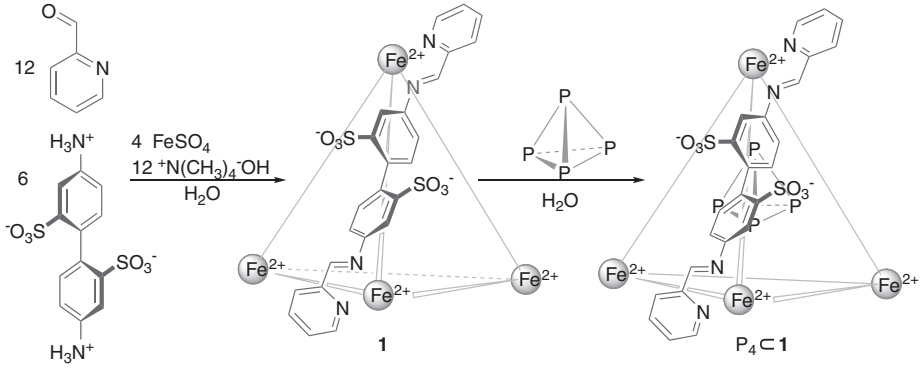

Fig. 1. Synthesis of tetrahedral cage **1** and subsequent incorporation of P_4.

[1]Department of Chemistry, University of Cambridge, Lensfield Road, Cambridge CB2 1EW, UK. [2]Department of Chemistry, Nanoscience Center, University of Jyväskylä, Post Office Box 35, 40014 JYU, Finland.

*To whom correspondence should be addressed. E-mail: jrn34@cam.ac.uk